

Decoupling of topology and texture in optical skyrmions under turbulence

D. G. Pires^{*} and N. M. Litchinitser[†]

Department of Electrical and Computer Engineering, Duke University, Durham, North Carolina 27708, USA

**danilo.gomes.pires@duke.edu*

†natalia.litchinitser@duke.edu

Abstract

Topological structure is widely invoked as a route to disorder-resilient photonic states, yet whether it protects locally resolved field structure under realistic disorder has not been established. Optical skyrmions, vectorial light fields characterized by a global skyrmion number N_{sk} , provide a stringent test of this question under turbulence. Although N_{sk} is expected to be robust, conservation of a global invariant does not guarantee preservation of the underlying polarization texture. Here we reconstruct the full Stokes field of optical skyrmions transmitted through controlled turbulent channels, combining experiment, phase screen simulations, and analytical modelling to independently track global and local observables. We demonstrate a broad disorder regime in which N_{sk} remains conserved while fine polarization structure rapidly degrades. This pronounced decoupling, strengthened for higher-order skyrmions, exposes a hierarchy of robustness between topological invariants and texture-resolved information, defining intrinsic limits of topological protection in disordered wave systems.

The ability to structure light in phase, polarization, and across space and time has opened new avenues for encoding information in its spatial and temporal degrees of freedom [1]. Many applications require propagation through environments that distort optical wavefronts, motivating the search for metrics that remain well-defined under perturbations [2]. Topology provides such metrics by treating an optical field as a mapping from physical coordinates to an internal state space that supports integer-valued invariants stable under smooth deformations [3]. These invariants offer compact labels of field structure that can persist even when conventional geometric measures fail. Atmospheric turbulence, however, introduces stochastic refractive-index fluctuations that cause scintillation, beam wander, and modal mixing [4–7], raising a central question: which structural metrics remain recoverable with sufficient fidelity after stochastic propagation?

Optical skyrmions provide a natural setting to address this question because they encode topology in polarization textures rather than scalar phase alone. Originally introduced in high-energy physics as topologically stable field configurations, skyrmions were later recognized as generic particle-like textures in ordered media [8–15]. In photonics, analogous structures can be engineered through superpositions of orthogonal polarization fields, periodic vector beams, spatiotemporal coupling, and fully three-dimensional vector fields [16–24]. This diversity makes them a versatile platform for testing the resilience of polarization-based topology relative to scalar structured beams [25–27]. Yet many applications rely not only on a conserved global invariant but also on the local texture that realizes it [18, 28, 29]. Here we disentangle these contributions using

a controlled turbulent channel, statistically matched split-step simulations, and an analytical scaling model. We show that the global skyrmion index remains stable across a broad disorder regime while texture-resolved metrics degrade. This separation becomes increasingly pronounced with higher texture order, leading to reduced ensemble-averaged fidelity and enhanced variance. Our analytical model captures both the robustness of low-order textures and the rapid degradation of higher-order ones, establishing a hierarchy of stability within topological light.

Global and local optical metrics distorted by turbulence

Atmospheric turbulence arises from mixing air parcels with different temperatures and humidity, producing random refractive-index fluctuations along an optical propagation path [30, 31]. These inhomogeneities accumulate as stochastic optical-path variations that introduce phase delays and convert them into amplitude modulations, beam spreading, and intensity scintillation. A common statistical description is provided by Kolmogorov theory, which models the turbulence as locally homogeneous and isotropic over an inertial range between outer and inner length scales [32]. Turbulence strength is typically characterized by the refractive-index structure parameter C_n^2 , enabling quantitative estimates of coherence loss and providing a basis for random phase-screen simulations. In the laboratory, turbulence is often emulated using programmable wavefront modulators driven by Kolmogorov statistics or with translated turbulence plates [33-36]. Here, we use a hot-air turbulence chamber to generate a distributed, dynamically evolving refractive-index distribution along the optical path [37]. Heater power and flow set the turbulence strength, which is calibrated from time-ensemble beam metrics to map experimental settings onto the Kolmogorov parameterization used in simulations (see Methods for chamber details).

These controlled realizations of atmospheric perturbations provide a direct route to investigate optical skyrmions, which are polarization textures defined by the spatial arrangement of the local polarization state across the beam cross-section. A convenient description maps each transverse point to a unit Stokes vector $\mathbf{s}(x, y) = \mathbf{S}/S_0$ on the Poincaré sphere, where $\mathbf{S} = (S_1, S_2, S_3)$ and S_0 are respectively the Stokes parameters and the total intensity. In this representation, the optical field forms a two-dimensional mapping into a closed order-parameter space. The associated skyrmion number is a global invariant that quantifies the degree of the mapping onto the sphere, and can be written as [16, 38]

$$N_{sk} = \frac{1}{4\pi} \iint_{\sigma} \mathbf{s} \cdot (\partial_x \mathbf{s} \times \partial_y \mathbf{s}) dx dy, \quad (1)$$

where the integrand is the local topological density and σ is the integration region. This formulation reflects the global nature of the invariant, suggesting that the skyrmion number can remain stable under moderate distortions. However, preservation of the global index does not, by itself, ensure the stability of the detailed polarization texture that encodes practical information. Optical skyrmions can be realized by superposing two co-propagating modes in orthogonal circular polarizations, formed from a Gaussian and a Laguerre-Gaussian (LG) mode, respectively, as $\mathbf{E}(r, \phi) = A_0 \text{LG}_0^0(r, \phi) \hat{\mathbf{e}}_R + A_m \text{LG}_0^m(r, \phi) e^{i\delta} \hat{\mathbf{e}}_L$, where $\hat{\mathbf{e}}_{R,L}$ denote right- (RCP) and left-

circular (LCP) polarization, m is the azimuthal winding number, and A_0, A_m, δ control the relative normalized weights and phase, respectively (detailed in Methods section). Figure 1 (a) shows a schematic of the experimental setup used to generate and probe the skyrmionic textures in turbulence (see Methods for details). Examples of the measured unperturbed and perturbed optical skyrmions are shown in Fig. 1(b) for Néel (b1, b4), Bloch (b2, b5), and anti-skyrmion (b3, b6) textures, respectively.

Beyond the global index, skyrmion textures are also characterized by local metrics that quantify the spatial structure of the polarization state within the cross-section. Expressing the Stokes vector in terms of spherical angles β, γ on the Poincaré sphere (see Section 1 of the Supplementary Materials for complete derivations) as $\mathbf{s} = (\sin \beta \cos \gamma, \sin \beta \sin \gamma, \cos \beta)$, one may define three local parameters [16, 38]. First, the polarity p , which characterizes the direction of the out-of-plane orientation near the texture center and at the boundary σ , is commonly defined as $P_{sk} = [\cos \beta(r_\sigma) - \cos \beta(0)]/2$. The second parameter is the vorticity $V_{sk} = (2\pi)^{-1} \int_0^{2\pi} \partial_\phi \gamma d\phi$, which quantifies the integer winding of the azimuthal angle γ around a closed loop enclosing the core. Finally, the third parameter is the helicity H_{sk} , which specifies the orientation of the in-plane rotation of (s_1, s_2) relative to the radial direction, and is defined as the offset between the texture angle and the geometric azimuth, $H_{sk} = \gamma - V_{sk} \phi$. Together, (P_{sk}, V_{sk}, H_{sk}) specify the local structure of the texture and distinguish different skyrmion types. For example, $(P_{sk}, V_{sk}, H_{sk}) = (1, 1, 0)$ and $(1, 1, \pi)$ correspond to Néel-type skyrmions, $(1, 1, \pm\pi/2)$ correspond to Bloch-type skyrmions, and $(1, -1, H_{sk})$ define anti-skyrmions for any H_{sk} .

Turbulence acts on these quantities through random refractive-index fluctuations that impose spatially varying phase delays and amplitude modulations, altering the relative phase and amplitude of the orthogonal polarization components across the beam. In physical terms, turbulence perturbs $\beta(x, y)$ and $\gamma(x, y)$ point by point, leading to core drift, local polarization rotation, and irregularities in the gradients $\partial_x \mathbf{s}$ and $\partial_y \mathbf{s}$. As a result, polarity becomes vulnerable when the area defining the core is displaced or obscured by intensity fluctuations. The vorticity is readily corrupted because it relies on coherent angular winding of γ , which turbulence can fragment by introducing spatially dependent relative-phase slips. The helicity is typically the most sensitive parameter, as it depends on a well-defined in-plane orientation that is strongly affected by local polarization distortions. On the other hand, the skyrmion number integrates the topological density over the full cross-section, so turbulence can strongly distort the local texture while leaving the net wrapping unchanged. Only sufficiently strong distortions produce large fluctuations in the integrated density or induce effective boundary leakage of the mapping. This separation between global robustness and local degradation motivates a focused examination of texture-level stability in turbulent channels.

Robustness of skyrmion textures under turbulence

Local texture metrics are extracted from the measured Stokes fields after turbulence by operating directly on $\mathbf{S} = (S_1, S_2, S_3)$ in the observation plane. The polarity P_{sk} is determined from the circular component of the Stokes parameters, using the mean value of S_3 at the texture core and at a reference radius that samples the outer region of the pattern. In practice, we evaluate S_3 at $r = 0$ and at the boundary $r = r_\sigma$ and assign the polarity from the relative orientation of these values [16, 38]. The texture-border radius r_σ was defined from the unperturbed skyrmion by selecting the radial location where the circular Stokes component S_3 undergoes its transition between $+1$ and -1 , providing a consistent reference boundary for all turbulence realizations. This definition remains effective under moderate distortions, but it becomes ambiguous when turbulence displaces the apparent core or suppresses contrast near r_σ . To address this issue, we employ an ensemble over realizations and an intensity-tracking algorithm to recenter the distorted field distribution with respect to its weighted intensity centroid. Across all the experimentally and numerically obtained textures, 100 realizations were performed for each turbulence strength. For each realization, the intensity centroid (x_m, y_m) is calculated upon evaluating $x_m = \iint xI(x, y)dxdy / I_0$ and $y_m = \iint yI(x, y)dxdy / I_0$, where $I(x, y)$ is the measured intensity and $I_0 = \iint I(x, y) dxdy$.

The vorticity V_{sk} is obtained from the azimuthal winding of the transverse Stokes complex field S_1 and S_2 , defined as $S_\perp = S_1 + iS_2 = |S_\perp| \exp(i\psi)$, where $\psi = \arg(S_\perp)$ is the in-plane polarization angle [16, 38]. We evaluate the integer circulation of ψ around the texture center as $V_{sk} = (2\pi)^{-1} \int_0^{2\pi} \partial_\phi \psi d\phi$. This procedure is closely analogous to extracting the topological charge of an OAM mode from the circulation of the optical phase [39]. Turbulence introduces spatially varying phase perturbations that redistribute power among neighboring winding numbers, leading to crosstalk between adjacent modes [4, 5, 33, 36]. In the present case, the random perturbation of ψ causes effective mixing among integer windings of the transverse polarization angle, so that the measured vorticity can fluctuate between realizations even when the global texture retains its overall topology. The analogy is therefore direct, where vorticity degradation represents the polarization-texture counterpart of OAM mode crosstalk, with the angle ψ playing the role of the scalar optical phase.

The helicity H_{sk} is estimated statistically by comparing the perturbed in-plane angle ψ to the corresponding unperturbed reference ψ_0 at matched spatial locations. We define an angular difference $\Delta\psi = \text{wrap}(\psi - \psi_0)$ on $(-\pi, \pi]$ and model its distribution with a von Mises probability density [40], which is the circular analogue of a normal distribution, written as $f(\Delta\psi; \mu, \kappa) = (2\pi I_0(\kappa))^{-1} \exp[\kappa \cos(\Delta\psi - \mu)]$. Here, μ is the mean direction, $\kappa \geq 0$ is the concentration parameter, and I_0 is the zeroth-order modified Bessel function of the first kind. In this framework, the mean helicity is identified with the fitted μ (or, equivalently, with the argument of the first circular moment), while κ quantifies how tightly the perturbed texture remains clustered around that mean. Specifically, if $\langle e^{i\Delta\psi} \rangle = R e^{i\mu}$, then $R \in [0, 1]$ measures circular coherence and is mapped to κ through the standard von Mises relation $R = I_1(\kappa) / I_0(\kappa)$. Turbulence broadens the $\Delta\psi$ distribution, which reduces R and drives κ downward, corresponding to a loss of a well-defined

H_{sk} even when a nonzero mean μ can still be identified over the ensemble (see Section 3 of the Supplementary Materials for details on this statistical model).

Figure 2 summarizes the values of the skyrmion number N_{sk} , polarity P_{sk} , vorticity V_{sk} , and helicity H_{sk} obtained numerically and experimentally for the first-order Néel- (a,d), Bloch- (b,e), and anti-skyrmion (c,f) textures over various turbulence strengths. The skyrmion number N_{sk} was computed directly from Eq. (1). As the turbulence strength increases, the persistence of N_{sk} alongside the rapid degradation of (P_{sk}, V_{sk}, H_{sk}) indicates that the polarization field retains its global wrapping on the Poincaré sphere even while the spatial organization that defines a recognizable texture is progressively disrupted. In other words, turbulence introduces transverse variations in the relative phase and amplitude between the orthogonal polarization components, which distort the gradients of the Stokes vector and redistribute the local topological density without necessarily altering its integral. This produces a regime where the global invariant remains measurable and close to its target value, yet the local structure required for encoding, classification, or tracking of textures becomes increasingly unreliable.

The loss of polarity at stronger turbulence has a direct geometrical meaning. The sign of S_3 at the core and at the edge r_σ no longer provides a stable up/down orientation of the texture. Experimentally, this occurs when the core position becomes uncertain, when intensity fluctuations reduce the fidelity of the Stokes reconstruction near the origin, or when the radial profile is reshaped so that the reference ring no longer samples the same portion of the texture. Once polarity becomes ambiguous, the texture can no longer be assigned to a well-defined central orientation, undermining any interpretation that depends on identifying a core state or distinguishing textures that differ only by the sense of their out-of-plane component.

Vorticity degradation reflects a breakdown of a coherent azimuthal progression of the transverse Stokes-field phase, denoted by $\arg(S_1 + iS_2)$. With increasing turbulence, the winding number extracted around a closed contour becomes realization-dependent because phase perturbations induce angular discontinuities and create or displace points where $|S_\perp|$ is small, effectively fragmenting the circulation. The resulting histograms in Fig. 2(d–f) are therefore the polarization-texture analogue of mode mixing in OAM channels, where the intended winding remains statistically favored, but weight is transferred to neighboring integers as the random medium strengthens. This redistribution has practical consequences for any scheme that uses vorticity as an information carrier, since it directly translates into symbol errors, even when N_{sk} still indicates that a nontrivial topology survives.

In addition, helicity exhibits a complementary form of fragility because it relies on a well-defined in-plane orientation relative to the reference texture. In the von Mises description, stronger turbulence broadens the distribution of angular differences, reducing the concentration parameter and driving the ensemble toward a nearly uniform angular distribution. In this regime, a mean helicity may still be formally defined, but it is no longer informative because the probability density is not localized around that mean value. This corresponds to a loss of a stable internal twist

direction of the texture, such that the distinction between Néel-like and Bloch-like arrangements becomes progressively obscured, even though the global mapping still wraps the sphere approximately once.

These observations clearly separate topological robustness from texture fidelity. The resilience of N_{sk} demonstrates that turbulence can preserve a global invariant even when polarity, vorticity, and helicity are no longer reliable metrics. Consequently, at stronger turbulence levels, the field may remain topologically nontrivial while carrying diminished usable texture information, suggesting that topology alone is insufficient to guarantee stability of the local features required for encoding and interpretation in realistic propagation channels.

Topological degradation of higher-order optical skyrmions

So far, measurements of first-order textures indicate that the global topological index can remain stable even after turbulence significantly distorts the spatial polarization pattern, supporting the use of N_{sk} as a robust metric in disturbed channels. However, does this resilience extend to higher-order optical skyrmions? To address this question, we examined Néel-type textures with increasing target order, propagating them through the same turbulent channel and retrieving N_{sk} in experiments and simulations. The combined results are shown in Fig. 3.

Across orders up to $N_{sk} = 5$, we find that the robustness of the skyrmion number is not universal. Instead, it becomes progressively reduced with increasing topological order. While low-order textures maintain near-constant N_{sk} over turbulence levels that already disrupt the local texture metrics, higher-order textures exhibit a significantly faster loss of a well-defined skyrmion number. This is evidenced by broadened distributions and a reduced probability of recovering the target skyrmion number. This behavior is consistent with the fact that higher-order textures contain finer spatial variation of the Stokes field and a more structured topological-density distribution. As a result, turbulence more readily redistributes density across the aperture and amplifies cancellation between positive and negative contributions in the integral defined in Eq. 1. Consequently, the global invariant can remain informative for modest orders, but it becomes increasingly susceptible to turbulence as the texture complexity grows. This limits the range over which topological protection can be reliably leveraged. A comparable order-dependent reduction in skyrmion-number fidelity has been reported previously, with a greater spread for more complex textures at higher background noise levels [41].

To quantify the loss of skyrmion-number fidelity with increasing texture order, we evaluated the degradation through the ensemble average $\langle N_{sk} \rangle$ and variance $\text{Var}(N_{sk})$ over many turbulence realizations. These metrics capture the fluctuations of the retrieved integer around its target value and therefore provide a direct measure of reliability without being obscured by outliers. Across the explored orders, $\langle N_{sk} \rangle$ decreases, while $\text{Var}(N_{sk})$ increases rapidly with respect to its initially unperturbed skyrmion number N_0 . This behavior reveals an exponential dependence that becomes evident already at moderate turbulence strengths, consistent with the observed broadening of the skyrmion-number distributions for higher-order textures. This trend is shown in Figs. 4 (a) and (b)

for $\sigma_R^2 = 0.25$ across numerical simulations and experiments, respectively, corresponding to the ensemble average and variance of N_{sk} .

We developed a model, treating the effective cumulative distortions as a multiplicative modulation of the topological-density field prior to integration, to interpret this scaling. For the complete derivation, refer to Section 4 of the Supplementary Materials. Using the Rytov-Tatarski description of turbulence-induced field fluctuations [30, 31], the resulting estimate predicts that the ensemble average of the skyrmion number decays as $\langle N_{sk} \rangle = N_0 \exp(\Lambda_{eff} N_0^2)$ and its variance grows as $\text{Var}(N_{sk}) = N_0^2 \exp(\Gamma_{eff} N_0^2)$, where $\Lambda_{eff} < 0$ and $\Gamma_{eff} > 0$ are effective turbulence parameters. As seen in Fig. 4, this exponential dependence accurately describes both numerical and experimental measurements. It also formalizes the order-dependent limitation on skyrmion-number resilience, even when the mean value remains near the target value at low orders. The retrieved values from the simulations (experiments) were $\Lambda_{eff}^{sim} = -0.008668$ ($\Lambda_{eff}^{exp} = -0.008481$) and $\Gamma_{eff}^{sim} = 0.15$ ($\Gamma_{eff}^{exp} = 0.21$), respectively. Although this theoretical model was developed to understand the correlations between the skyrmion number and perturbations from atmospheric turbulence, it can be further modified to study other optical stochastic systems. Besides the clear analogy to the behavior of higher OAM scalar modes in turbulence [4, 5, 33, 36, 42], similar order-dependent limitations are reported in dilute Bose-Einstein condensates [43] and nematic liquid crystals [44]. In the present context, these precedents reinforce that increasing topological order does not automatically strengthen or maintain equal protection.

Methods

Convective-air turbulence chamber

The turbulence chamber used in the experiments generates a controlled volume of turbulent airflow with an internal mixing region measuring approximately $150 \times 150 \times 150 \text{ mm}^3$ in a rectangular cuboid shape. Ambient air is driven into the chamber by two fans, while a third fan injects a heated stream; a separate exhaust fan maintains a steady throughflow and promotes continuous mixing. The optical beam enters and exits through dedicated apertures and experiences time-dependent wavefront distortions as refractive-index fluctuations evolve within the volume. The heated air source can reach 120°C with a temperature stability of approximately $\pm 0.1^\circ\text{C}$. Under these operating conditions, the characteristic temporal bandwidth of the transverse flow corresponds to a Greenwood frequency of $f_G \approx 35 \text{ Hz}$. It contains 4 circular optical ports with a diameter of about 76.2 mm located at each side of the chamber, which are used to reflect the structured light multiple times using mirrors.

Optical skyrmionic textures

Optical skyrmions were prepared as paraxial vector fields formed by the coherent addition of two spatial modes carried by orthogonal circular polarizations. The circular basis vectors are defined

as $\hat{\mathbf{e}}_R = (\hat{\mathbf{x}} - i\hat{\mathbf{y}})/\sqrt{2}$ and $\hat{\mathbf{e}}_L = (\hat{\mathbf{x}} + i\hat{\mathbf{y}})/\sqrt{2}$. The skyrmionic complex envelope is written as [38, 41]

$$\mathbf{E}(r, \phi) = E_R(r, \phi, z) \hat{\mathbf{e}}_R + E_L(r, \phi, z) \hat{\mathbf{e}}_L, \quad (2)$$

with $E_R = A_0 \text{LG}_0^0(r, \phi, z)$ and $E_L = A_m \text{LG}_0^m(r, \phi, z) e^{i\delta}$. Here, LG_0^0 denotes the fundamental Gaussian mode, LG_0^m is an LG mode with azimuthal index m and null radial orders, A_0 and A_m set the relative normalized weights, and δ controls the relative phase between the two circular components. In standard notation, $\text{LG}_0^m(r, \phi, z) = U_m(r, z) e^{im\phi}$, where $U_m(r, z)$ is the spatial envelope determined by the beam waist and propagation distance, given by [45]

$$U_m(r, z) = \sqrt{\frac{2}{\pi|m|!}} \frac{1}{w(z)} \left(\frac{\sqrt{2}r}{w(z)} \right)^{|m|} e^{-\frac{r^2}{w(z)^2}} e^{-i\frac{kr^2}{2R(z)}} e^{i(|m|+1)\zeta(z)}, \quad (3)$$

with the beam size $w(z) = w_0 \sqrt{1 + (z/z_R)^2}$, wavefront radius of curvature $R(z) = z[1 + (z_R/z)^2]$, and the Gouy-phase-term factor $\zeta(z) = \text{atan}(z/z_R)$. In all previous expressions, $z_R = kw_0^2/2$ is the Rayleigh range and w_0 is the minimum beam waist.

The resulting spatially varying superposition converts the azimuthal phase factor $e^{im\phi}$ into a polarization texture through the interference between the RCP and LCP components. From \mathbf{E} , the Stokes parameters $\mathbf{S} = (S_1, S_2, S_3)$ are obtained as $S_0 = |E_R|^2 + |E_L|^2$, $S_1 = |E_x|^2 - |E_y|^2$, $S_2 = |E_a|^2 - |E_d|^2$, and $S_3 = |E_R|^2 - |E_L|^2$. Here, E_x, E_y, E_a, E_d correspond respectively to the horizontal, vertical, antidiagonal, and diagonal components of the vector field. The unit Stokes vector $\mathbf{s} = \mathbf{S}/S_0$ provides a map $(x, y) \rightarrow \mathbf{s}(x, y)$ that defines the skyrmion texture. The order of the texture is controlled primarily by the integer m , while the parameters A_m/A_0 and δ are chosen to set the radial extent of the transition in S_3 and the in-plane orientation of the transverse Stokes component, enabling reproducible preparation of the target skyrmion type at the input plane.

Atmospheric phase screens

Atmospheric turbulence was modeled numerically by sampling two-dimensional stochastic phase masks whose second-order statistics follow Kolmogorov scaling [30-32, 42, 46]. We define the phase structure function as $\Psi(\mathbf{r}) = \langle |\Phi(\mathbf{r}' - \mathbf{r}) - \Phi(\mathbf{r}')|^2 \rangle$, with $\langle \cdot \rangle$ denoting the ensemble average of a random phase screen Φ , and relate it to a spatial-frequency power spectrum $\Theta(\boldsymbol{\kappa})$ through the standard Fourier relationship for stationary random processes. For Kolmogorov turbulence, the spectrum is evaluated from the Wiener spectrum Θ as [37, 42, 46]

$$\Psi(\mathbf{r}) = 2 \int \Theta(\boldsymbol{\kappa}) [1 - \cos(2\pi\boldsymbol{\kappa} \cdot \mathbf{r})] d^2\boldsymbol{\kappa} = 6.88 \left(\frac{|\mathbf{r}|}{r_0} \right)^{5/3}, \quad (4)$$

where $\Theta(\boldsymbol{\kappa}) = 0.023r_0^{-5/3} |\boldsymbol{\kappa}|^{-11/3}$, r_0 is the Fried parameter that sets the turbulence strength. Alternatively, Θ represents the covariance function of the random power spectrum $P(\boldsymbol{\kappa}) = \int \Theta(\boldsymbol{\kappa}) \exp[-i2\pi\boldsymbol{\kappa} \cdot \mathbf{r}] d^2\mathbf{r}$. Phase screens are synthesized by a spectral sampling procedure on an

$N \times N$ grid spanning an aperture size D . A complex Gaussian random array $M(\boldsymbol{\kappa})$ (zero mean, unit variance) is generated on the discrete frequency lattice and shaped by the target spectrum as $P(\boldsymbol{\kappa}) = \sqrt{\Theta(\boldsymbol{\kappa})} M(\boldsymbol{\kappa})$ [46, 47]. The corresponding phase realization is obtained by an inverse Fourier transform, taking the real component, $\Phi(x, y) = \Re\{\mathcal{F}^{-1}[P(\boldsymbol{\kappa})]\}$. Because the smallest resolvable frequency on the grid is $1/D$, this direct sampling underrepresents large-scale contributions associated with the $\kappa^{-11/3}$ dependence. We therefore augment the screen with additional low-frequency components by evaluating the spectrum at frequencies below $1/D$ and adding the resulting long-period Fourier terms with independent random coefficients. This correction restores the slowly varying content of the phase maps and improves agreement with Kolmogorov statistics over the full range of spatial scales supported by the simulation grid.

Experimental setup

To quantify how the skyrmionic global and local optical metrics get affected by turbulence in experiments, a continuous-wave laser tuned at $\lambda = 532$ nm illuminates a spatial light modulator (Hamamatsu LCOS-SLM X15213-01) at the holographic modulation section, modulating the incoming beam into a pair of optical modes carrying a LG and Gaussian mode profiles, respectively. Here, a hologram is generated using an approximated inverse-sinc technique to achieve amplitude and phase control [48]. The generated modes are spatially superposed with orthogonal linear polarization upon inserting a half-wave plate (HWP) in one of the arms and filtered with an iris (I) to obtain a single LG mode in one arm and a single Gaussian mode in the other arm, then routed to propagate within the turbulence chamber. At the chamber entrance, a quarter-wave plate (QWP) converts the orthogonal linear polarization states into the corresponding circular polarization states, RCP and LCP. After the propagation, a beam splitter (BS) divides the beam into two routes, where a QWP is inserted in one arm. A polarization-resolved camera (Allied Vision Mako G-508B POL) is used to obtain the complete Stokes measurements at single shot, where the arm with the QWP allows the acquisition of the RCP/LCP states, while the other arm directly measures all four linear polarization components, *i.e.*, horizontal, vertical, diagonal, and anti-diagonal states, which are numerically superposed during the data analysis referenced by the intensity centroid, as discussed in the main text. This method of acquisition is particularly efficient for single-shot measurements of the Stokes parameters when time-varying media are used [49]. To emulate long propagation distances in turbulence, the Fresnel scaling number $F = w_0^2/\lambda L$ ensures that the experimental arrangement is compatible with the evolution of a $w_0 = 6$ mm beam size ($1/e^2$) over a $L = 270$ m turbulence channel [37, 42, 49]. Here, w_0 is the beam waist radius, λ the wavelength of the light, and L the channel length. In the laboratory frame, the distance of $L_{lab} = 1.5$ m is achieved by using mirrors to reflect the beam multiple times within the turbulence chamber at different internal positions.

Numerical simulations

Numerically, we reproduce the experiment using split-step propagation through multiple statistically independent phase screens drawn from a Kolmogorov spectrum, separated by free-

space propagation segments. Here, the $w_0 = 6$ mm beam is propagated over the $L = 270$ m channel. The number of phase screens N_{sc} is chosen so that each step corresponds to a weak interaction, while the cumulative distortion matches the target turbulence strength, following $N_{sc} = (10\sigma_R^2)^{-6/11}$ [50]. The Rytov variance is defined as $\sigma_R^2 = 1.23C_n^2 k^{7/6} L^{11/6}$, where $k = 2\pi/\lambda$ is the wavenumber, while C_n^2 and L were previously defined. To align laboratory settings with simulation parameters, the chamber is calibrated by monitoring intensity fluctuations of a Gaussian beam and estimating the values of C_n^2 from the beam wander at various temperature regimes. For more details, we present the calibration curve and the calculations used to estimate C_n^2 from experiments in Section 2 of the Supplementary Materials. The simulated fields are then processed with the same polarization reconstruction and topological analysis pipelines used for experimental measurements.

Data availability. The data that support the findings of this study are available from the corresponding author upon reasonable request.

Code availability. The code used to produce the figures is available from the corresponding author upon reasonable request.

Acknowledgements. This work was supported by the Army Research Office (W911NF2310057). We thank H. Barati Sedeh and J. Tan for the fruitful discussions.

Author contributions. N.L. and D.G.P. formulated the concept of this study, performed theoretical and numerical analysis, and interpreted the results. D.G.P. designed and operated the experiments. All authors contributed to the discussion of the results and writing of the manuscript.

Competing interests. The authors declare no competing interests.

References

1. He, C., Y. Shen, and A. Forbes, *Towards higher-dimensional structured light*. Light: Science & Applications, 2022. **11**(1): p. 205.
2. Cox, M.A., et al., *Structured light in turbulence*. IEEE Journal of Selected Topics in Quantum Electronics, 2020. **27**(2): p. 1-21.
3. Soskin, M., et al., *Singular optics and topological photonics*. 2017, IOP Publishing. p. 010401.
4. Li, S., et al., *Atmospheric turbulence compensation in orbital angular momentum communications: Advances and perspectives*. Optics Communications, 2018. **408**: p. 68-81.
5. Malik, M., et al., *Influence of atmospheric turbulence on optical communications using orbital angular momentum for encoding*. Optics Express, 2012. **20**(12): p. 13195-13200.
6. Rodenburg, B., et al., *Influence of atmospheric turbulence on states of light carrying orbital angular momentum*. Optics Letters, 2012. **37**(17): p. 3735-3737.
7. Tyler, G.A. and R.W. Boyd, *Influence of atmospheric turbulence on the propagation of quantum states of light carrying orbital angular momentum*. Optics Letters, 2009. **34**(2): p. 142-144.

8. Perring, J. and T. Skyrme, *A model unified field equation*. Nuclear Physics, 1962. **31**: p. 550-555.
9. Skyrme, T., *A non-linear theory of strong interactions*. Proceedings of the Royal Society of London. Series A. Mathematical and Physical Sciences, 1958. **247**(1249): p. 260-278.
10. Skyrme, T., *A unified model of K-and π -mesons*. Proceedings of the Royal Society of London. Series A. Mathematical and Physical Sciences, 1959. **252**(1269): p. 236-245.
11. Skyrme, T., *Particle states of a quantized meson field*. Proceedings of the Royal Society of London. Series A. Mathematical and Physical Sciences, 1961. **262**(1309): p. 237-245.
12. Skyrme, T.H.R., *A non-linear field theory*. Proceedings of the Royal Society of London. Series A. Mathematical and Physical Sciences, 1961. **260**(1300): p. 127-138.
13. Skyrme, T.H.R., *A unified field theory of mesons and baryons*. Nuclear Physics, 1962. **31**: p. 556-569.
14. Han, J.H., et al., *Skyrmion lattice in a two-dimensional chiral magnet*. Physical Review B—Condensed Matter and Materials Physics, 2010. **82**(9): p. 094429.
15. Muhlbauer, S., et al., *Skyrmion lattice in a chiral magnet*. Science, 2009. **323**(5916): p. 915-919.
16. Shen, Y., et al., *Optical skyrmions and other topological quasiparticles of light*. Nature Photonics, 2024. **18**(1): p. 15-25.
17. Teng, H., et al., *Construction of optical spatiotemporal skyrmions*. Light: Science & Applications, 2025. **14**(1): p. 324.
18. Tsesses, S., et al., *Optical skyrmion lattice in evanescent electromagnetic fields*. Science, 2018. **361**(6406): p. 993-996.
19. Wang, B., et al., *Topological water-wave structures manipulating particles*. Nature, 2025. **638**(8050): p. 394-400.
20. Yang, A., et al., *Optical skyrmions: from fundamentals to applications*. Journal of Optics, 2025. **27**(4): p. 043002.
21. Pires, D.G. et al., *Structuring polarization states of light in space and time*. Nanophotonics, 2025. **14**(24): p. 4377-4385.
22. Putley, H.J., et al., *Mixing skyrmions and merons in topological quasicrystals of the evanescent optical field*. Optica, 2025. **12**(5): p. 614-619.
23. Du, L., et al., *Deep-subwavelength features of photonic skyrmions in a confined electromagnetic field with orbital angular momentum*. Nature Physics, 2019. **15**(7): p. 650-654.
24. Smirnova, D.A., F. Nori, and K.Y. Bliokh, *Water-wave vortices and skyrmions*. Physical Review Letters, 2024. **132**(5): p. 054003.
25. Wang, A.A., et al., *Topological protection of optical skyrmions through complex media*. Light: Science & Applications, 2024. **13**(1): p. 314.
26. Zhang, Z., et al., *Topological protection degrees of optical skyrmions and their electrical control*. Photonics Research, 2025. **13**(9): p. B1-B11.
27. Guo, Z., et al., *Topological robustness of classical and quantum optical skyrmions in atmospheric turbulence*. Nature Communications, 2026.
28. Kumar, V. and N.K. Viswanathan, *Topological structures in vector-vortex beam fields*. Journal of the Optical Society of America B, 2014. **31**(6): p. A40-A45.
29. D'Errico, A. et al., *Topological features of vector vortex beams perturbed with uniformly polarized light*. Scientific Reports, 2017. **7**(1): p. 40195.

30. Andrews, L.C. and R.L. Phillips, *Laser beam propagation through random media*. Laser Beam Propagation Through Random Media: Second Edition, 2005.
31. Tatarski, V.I., R.A. Silverman, and N. Chako, *Wave propagation in a turbulent medium*. 1961, American Institute of Physics.
32. Lane, R., A. Glindemann, and J. Dainty, *Simulation of a Kolmogorov phase screen*. Waves in random media, 1992. **2**(3): p. 209.
33. Ren, Y.X., et al., *Adaptive optics compensation of multiple orbital angular momentum beams propagating through emulated atmospheric turbulence*. Optics Letters, 2014. **39**(10): p. 2845-2848.
34. Anzuola, E. and A. Belmonte, *Generation of atmospheric wavefronts using binary micromirror arrays*. Applied Optics, 2016. **55**(11): p. 3039-3044.
35. Cox, M.A., et al., *A High-Speed, Wavelength Invariant, Single-Pixel Wavefront Sensor With a Digital Micromirror Device*. IEEE Access, 2019. **7**: p. 85860-85866.
36. Ren, Y.X., et al., *Atmospheric turbulence effects on the performance of a free space optical link employing orbital angular momentum multiplexing*. Optics Letters, 2013. **38**(20): p. 4062-4065.
37. Pires, D., et al., *Stability of optical knots in atmospheric turbulence*. Nature Communications, 2025. **16**(1): p. 3001.
38. Shen, Y., E.C. Martínez, and C. Rosales-Guzmán, *Generation of optical skyrmions with tunable topological textures*. Acs Photonics, 2022. **9**(1): p. 296-303.
39. Berry, M., *Optical vortices evolving from helicoidal integer and fractional phase steps*. Journal of Optics A: Pure and Applied Optics, 2004. **6**(2): p. 259-268.
40. Mardia, K.V. and P.E. Jupp, *Directional statistics*. 2009: John Wiley & Sons.
41. McWilliam, A., et al., *Topological approach of characterizing optical skyrmions and multi-skyrmions*. Laser & Photonics Reviews, 2023. **17**(9): p. 2300155.
42. Peters, C., V. Cocotos, and A. Forbes, *Structured light in atmospheric turbulence—a guide to its digital implementation: tutorial*. Advances in Optics and Photonics, 2025. **17**(1): p. 113-184.
43. Shin, Y.-i., et al., *Dynamical instability of a doubly quantized vortex in a Bose-Einstein condensate*. Physical Review Letters, 2004. **93**(16): p. 160406.
44. Susser, A.L., et al., *Transition from escaped to decomposed nematic defects, and vice versa*. Soft matter, 2020. **16**(20): p. 4814-4822.
45. Allen, L., et al., *Orbital angular momentum of light and the transformation of Laguerre-Gaussian laser modes*. Physical Review A, 1992. **45**(11): p. 8185.
46. Burger, L., I.A. Litvin, and A. Forbes, *Simulating atmospheric turbulence using a phase-only spatial light modulator*. South African Journal of Science, 2008. **104**(3): p. 129-134.
47. Fried, D.L., *Optical resolution through a randomly inhomogeneous medium for very long and very short exposures*. JOSA, 1966. **56**(10): p. 1372-1379.
48. Bolduc, E., et al., *Exact solution to simultaneous intensity and phase encryption with a single phase-only hologram*. Optics Letters, 2013. **38**(18): p. 3546-3549.
49. Peters, C., et al., *The invariance and distortion of vectorial light across a real-world free space link*. Applied Physics Letters, 2023. **123**(2).
50. Xiao, X. and D. Voelz, *On-axis probability density function and fade behavior of partially coherent beams propagating through turbulence*. Applied optics, 2009. **48**(2): p. 167-175.

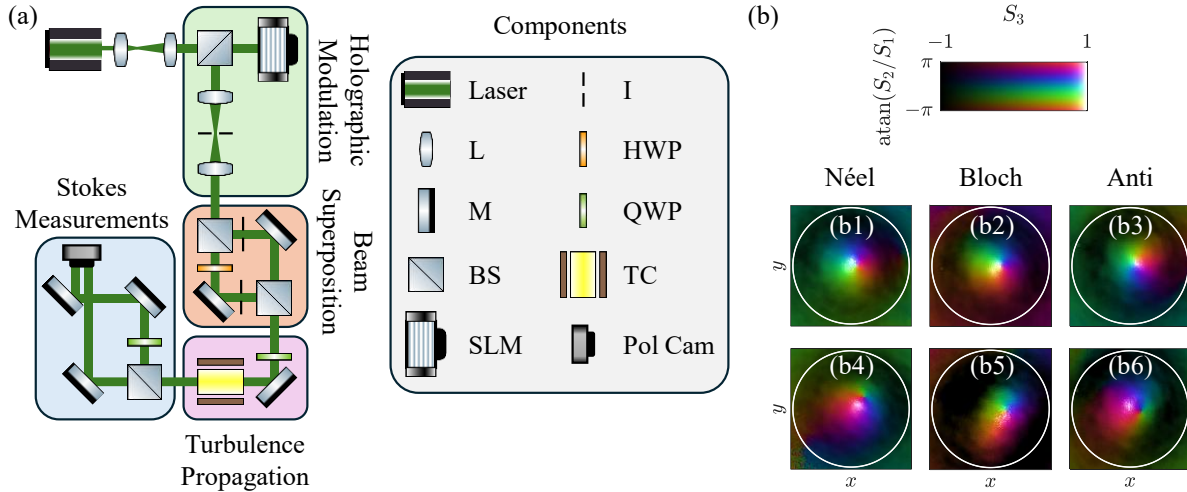


Fig 1. Experimental arrangement. **a** The LG and Gaussian modes are generated in experiments using a phase-only SLM in the Holographic Modulation section, overlapped in the Beam Superposition section, then routed to the chamber in the Turbulence Propagation section. Single-shot acquisition of the polarization information is realized in the Stokes Measurements section using a polarization-sensitive camera. The labels correspond to: L lens, M mirror, BS beamsplitter, SLM spatial light modulator, I iris, HWP half-wave plate, QWP quarter-wave plate, TC turbulence chamber, Pol Cam polarization-sensitive camera. **b** Examples of the measured Néel- (b1, b4), Bloch- (b2, b5), and anti-skyrmion (b3, b6) textures, where the first row indicates the distributions without perturbation and the second row corresponds to the cases for $\sigma_R^2 = 0.25$ ($T = 70^\circ\text{C}$), respectively. The color scheme indicates the complete unit Stokes vector $\mathbf{s} = (s_1, s_2, s_3)$, and the white circle is the region of integration σ .

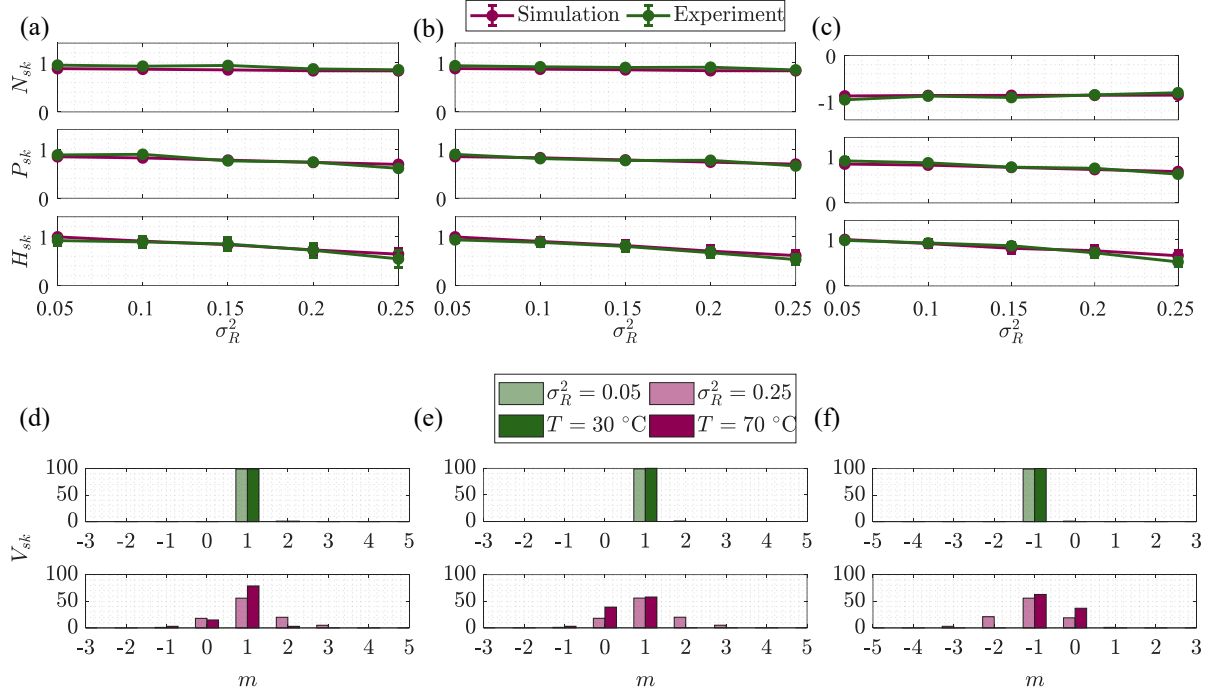


Fig. 2. Robustness of global and local parameters to turbulence. **a-c** Retrieved skyrmion number N_{sk} , polarity P_{sk} , and helicity H_{sk} values from simulations (pink) and experiments (green) across various turbulence strength levels, denoted by the Rytov variance σ_R^2 . From left to right, each panel corresponds to the Néel-, Bloch-, and anti-skyrmions, respectively. The error bars correspond to the standard error across the 100 realizations. **d-f** Histogram distributions for the vorticity V_{sk} obtained for turbulence levels $\sigma_R^2 = 0.05$ ($T = 30^\circ\text{C}$) and $\sigma_R^2 = 0.25$ ($T = 70^\circ\text{C}$), here addressed by the green and pink colors, respectively. Light colors refer to simulations, while dark colors represent the experimental results. From left to right, each panel corresponds to the Néel-, Bloch-, and anti-skyrmions, respectively. In all histograms, the parameter m denotes the measured winding number across the statistical realizations.

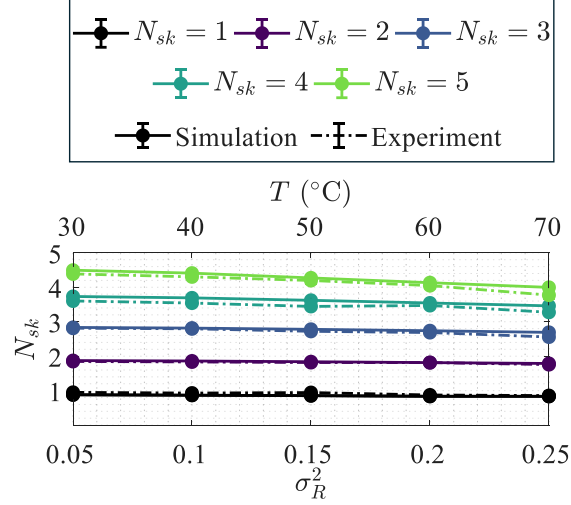


Fig. 3. Stability of higher-order topologies. Skyrmion number N_{sk} inferred from simulations (solid lines) and experiments (dashed lines) for various topological orders, propagating a Néel-type skyrmion with skyrmion number spanning from $N_{sk} = 1, \dots, 5$. The Rytov variance axis σ_R^2 corresponds to the turbulence strength parameter for the simulation results, while the temperature T axis refers to the experiments. The error bar is the standard error across 100 realizations for each point.

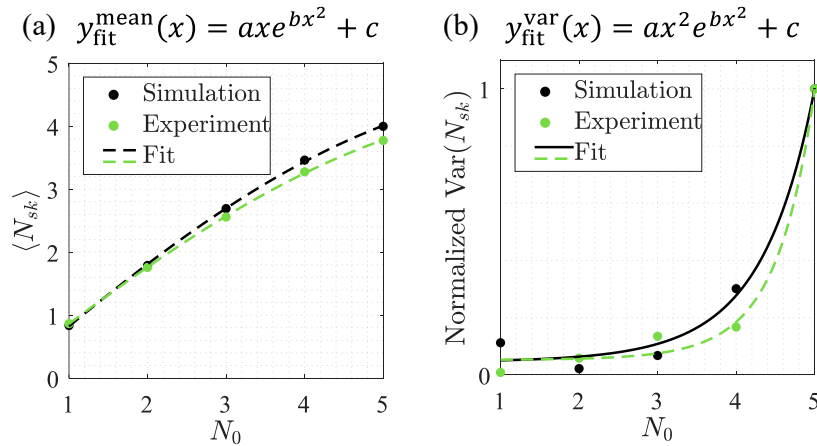


Fig. 4. Uncertainty of higher-order skyrmion number predictions. (a) Ensemble average and (b) normalized variance of the skyrmion number values ensembled across simulation (black dots) and experiment (green dots) for $N_0 = 1, \dots, 5$ and turbulence level $\sigma_R^2 = 0.25$ ($T = 70^\circ\text{C}$) from Fig. 3. The fitting curves for the simulation (black solid line) and experimental (dashed green line) results with function (a) $y(x) = axe^{bx^2} + c$ and (b) $y(x) = ax^2e^{bx^2} + c$, respectively showing an exponential response in the variance of retrieved skyrmion numbers with respect to the initial topological order. In panel (b), the simulation and experimental results are normalized to their own maximum $\text{Var}(N_{sk})$ values.